Nanoscale

Chiral Metamaterials via Moiré Stacking

Journal:	*Nanoscale*
Manuscript ID	NR-FEA-05-2018-004352.R1
Article Type:	Feature Article
Date Submitted by the Author:	05-Jul-2018
Complete List of Authors:	Wu, Zilong; The University of Texas at Austin, Texas Materials Institute Liu, Yaoran; The University of Texas at Austin Hill, Eric; The University of Texas at Austin Zheng, Yuebing; The University of Texas at Austin, Department of Mechanical Engineering

Chiral Metamaterials via Moiré Stacking

Zilong Wu[#], *Yaoran Liu*[#], *Eric H. Hill, Yuebing Zheng**

Department of Mechanical Engineering, Materials Science and Engineering Program, and Texas Materials Institute

The University of Texas at Austin, Austin, Texas 78712, United States

E-mail: zheng@austin.utexas.edu

[#] These authors contributed equally to this work.

Keywords: moiré patterns, metamaterials, metasurfaces, moiré chiral metamaterials, chirality, chiroptical effects

Abstract

Chiral metamaterials have attracted strong interest due to their versatile capabilities in spin-dependent light manipulation. Benefiting from advancements in nanofabrication and mechanistic understanding of chiroptical effects, chiral metamaterials have shown potential in a variety of applications including circular polarizers, chiral sensors, and chiroptical detectors. Recently, chiral metamaterials made by moiré stacking, superimposing two or more periodic patterns with different lattice constants or relative spatial displacement, have shown promise for chiroptical applications. The moiré chiral metamaterials (MCMs) take advantage of lattice-dependent chirality, giving cost-effective fabrication, flexible tunability, and reconfigurability superior to conventional chiral metamaterials. This feature article focuses on recent progress of MCMs. We discuss optical mechanisms, structural design, fabrication, and applications of the MCMs. We conclude with our perspectives on the future opportunities for the MCMs.

1. Introduction

1.1 Chiroptical effects and applications

Chirality is a geometrical phenomenon describing two objects with mirror symmetry that cannot be superimposed. The most commonly observed chirality is exhibited in human bodies, where hands are mirrored images of each other. Therefore, chirality is also known as handedness. Chiral molecules are usually termed as left-handed (LH) or right-handed (RH) enantiomers, depending on their structural chirality. Although chirality has been scientifically defined by Lord Kelvin more than a hundred years ago,[1] it has attracted increasing attention in recent decades due to the discovery of dominant roles of chirality in nature. For example, chiral molecules are the building blocks of life. Many biologically active molecules such as amino acids, drugs, sugars, and enzymes exhibit chirality.[2, 3] The prevalence of one enantiomer over its mirror image has been touted as a means to look for signs of life in interstellar exploration.[4-6] In particular, the study of chirality of amino acids in cometary and interstellar ice has given a deep understanding of the origin of life on Earth.[7] Chirality also determines many biological properties of chiral molecules. For example, fruit juices should contain only one enantiomer of amino acids, which are essential to human nutrition.[8] The handedness of enantiomers of limonene also determines whether the aroma is of orange or lemon. More importantly, cells use D-glucose rather than L-glucose as an energy source, making L-glucose a low-calorie sweetener for patients with diabetes mellitus.

Chirality can induce interesting optical activities in chiral entities. The asymmetric interactions between circularly polarized light (CPL) and materials with structural chirality can generate chiroptical effects, including optical rotation dispersion (ORD) and circular dichroism (CD). Both ORD and CD have been applied to characterize optical chirality of chiral entities: the former describes the capability of chiral materials to rotate the polarization of incident light, while the latter describes the asymmetric extinction of LH and RH CPL passing through chiral materials. Since the discovery of chiroptical responses in 1848,[9] the significance of optical chirality has been increasingly revealed. One hypothetical origin of the biomolecular homochirality on Earth has been proposed to be astronomical sources of circularly polarized light.[10] The asymmetric photoreactions of biomolecules on Earth irradiated by circularly polarized ultraviolet light may have led to enantiomeric excess in a racemic mixture of chiral entities.[11] In addition, chiroptical properties can be observed in many living creatures, which have developed adaptations to control CPL through evolution. For example, *Chrysina gloriosa*, a species of iridescent green beetle, has developed cell patterns on their exoskeletons that are structurally and optically analogous to a cholesteric liquid crystal, leading to selective reflection of CPL.[12] Helicoidal structures, which transmit RH CPL but reflect LH CPL, can also be observed in decalcified crustacean cuticle.[13] The polarimetry of the circularly polarizing cuticle of scarab beetles has attracted strong interest to understand the survival value provided by optical chirality of such components in many creatures.[14, 15] Circularly polarized scattering has been observed in single dinoflagellates and suspensions thereof, which can be applied to enhance image contrast in underwater imaging.[16] Besides alternating and utilizing the polarization of background light, biological objects can also emit light with circular polarization. For example, both CD in extinction and circular polarization in fluorescence have been observed in chlorophyll due to the chiral organization of chlorophyll molecules, which influences the photosynthesis apparatus.[17] Circular polarization is also observed in bioluminescence of fireflies of *Photuris spp*.[18]

Chiroptical responses of chiral materials have also played significant roles in an ever-increasing number of applications. Optical chirality has proven to be an effective way to solve the difficulty of detecting structural handedness of chiral molecules. Due to the same composition of atomic elements and symmetric chemical bonds, enantiomers of many chiral molecules show indistinguishable physical and chemical properties, which are dependent on scalar interactions in most cases. Vector-dependent or chirality-dependent interactions are therefore required to analyze and even separate the enantiomers of chiral molecules. The asymmetric CPL absorption of chiral molecules leads to opposite signs in CD or ORD spectra for enantiomers with different handedness, therefore enabling the detection of their chirality.[19, 20] Chiral molecules have been enantioselectively distinguished by chirality-dependent binding of enantiomers to chiral agents. Incident light with circular polarization can provide similar chirality-dependent "binding" to molecular enantiomers, but without the demand for chemical binding agents. Such chiroptical characterization and separation have been widely applied in such areas as chemistry, food analysis, and drug development.[3, 21-23]

Growing knowledge of chiroptical responses has enabled the development of chiral films to manipulate and use CPL for a wide range of applications. Hodgkinson et al. developed LH titanium oxide chiral films with large optical activity using serial deposition technology.[24] Based on a similar method, Wu et al. achieved a chiral titanium oxide coating with screw-like LH nanostructures for chiral reflectors or filters which reflect LH light but transmit RH light with near-unity efficiency.[25] Chiral filters based on the chirality of materials or nanostructures have also been developed using such techniques as tandem thin film coating, Fabry-Perot chiral cavities, and circular Bragg resonance.[26-28] The large circular birefringence of chiral films has shown potential for more sophisticated light manipulation. For example, a chiral film on an unpolarized light emitting diode has been effective in enhancing the CPL emission.[29] Combining film chiral filters with imaging pixels has led to chiral detectors.[30]

1.2 Chiral metamaterials

Although chiroptical materials and devices can be obtained by aggregation of chiral molecules or controlled deposition of inorganic materials, these natural materials face challenges to meet the requirements of emerging applications, which call for both strong chiroptical effects and ease of on-chip integration. Most natural chiral molecules show chiroptical responses in ultraviolet (UV) or deep-UV, limiting their applications in chiroptical devices that operate on visible and infrared light.[31] In addition, the large scalar discrepancy between sizes of chiral molecules and wavelengths of electromagnetic waves leads to weak interactions of light with the chiral molecules. Therefore, the chiral birefringence of most natural chiral molecules is below 0.1%, which is often not large enough for practical device.[32] On the contrary, chiral films of inorganic materials provide strong chiroptical responses with tunable working wavelengths from the visible to near-infrared regime.[29] However, such films are usually very thick in order to achieve strong optical chirality, which are too bulky for nanophotonic devices such as on-chip polarizers, light sources, and detectors.

The rapid development of nanotechnology in recent decades has provided promising solutions to novel chiral materials. Emerging nanophotonic effects such as surface plasmons and photonic cavities have been used to induce strong interactions between incident light and individual engineered nanoscale or microscale structures, which are known as meta-atoms.[33-37] In plasmonic meta-atoms, the resonant oscillations of free electrons driven by incident light have enabled extraordinary light manipulation capabilities, leading to slow light effects, sub-wavelength electromagnetic field localization, and efficient optical heating.[38-40] The dielectric counterparts of plasmonic meta-atoms such as silicon particles can confine incident light and generate standing waves by utilizing strong reflections at the interface between low-refractive-index environments and high-refractive-index particles.[41-44] The strong light confinement in dielectric cavities is usually attributed to Mie resonances.[45-47] Design and arrangement of meta-atoms as building blocks in three-dimensional (3D) structures lead to optical metamaterials. Benefiting from the collective optical resonances of meta-atoms, metamaterials have shown more sophisticated capabilities for light manipulation with enhanced performances. For example, near-unity optical absorption can be achieved by metamaterials with thickness smaller than 1/10 of wavelength of incident light.[48-50] The optical responses of metamaterials, including operation wavelength and line-shape, can be precisely controlled by tuning the size, shape and arrangement of the meta-atoms.[51-54] More importantly, the strongly enhanced light-matter interactions have enabled metamaterials with novel optical properties that are not achievable in natural materials. For example, negative refractive indices have been achieved in metamaterials with double-fishnet structures, double-layer of hole arrays, and metal wire arrays.[34, 55-57] The extraordinary capabilities of metamaterials in controlling the effective refractive index and light propagation have led to the realization of optical cloaking.[56, 58] The arrangement of dielectric optical cavities into metamaterials with face-centered cubic or hexagonal close-packed crystal structures has also led to interesting photonic band structures.[59, 60]

Planar two-dimensional (2D) versions of metamaterials, which are arrays of meta-atoms on 2D surfaces, are known as metasurfaces.[35, 37] Benefiting from the collective light-matter interactions of meta-atoms in a 2D arrangement, ultrathin metasurfaces have shown extraordinary capabilities for light manipulation for highly integrated photonic devices. For example, both plasmonic and dielectric metasurfaces have been used as meta-lenses, which can break the limits of resolution and numerical aperture in conventional optical lenses.[61-64] Well-engineered electromagnetic hot spots and ultranarrow spectral line shapes of metasurfaces have also been achieved to enable ultrasensitive biological or chemical sensing.[65-67] Moreover, multiple optical modes can be generated in a single metasurface to induce Fano resonances and strong coupling, which are promising for sensing at the single-molecule level.[67, 68]

Chiral metamaterials and metasurfaces with strong chiroptical responses are emerging. The strongly enhanced light-matter interactions at meta-atoms leads to chiral metamaterials with chiroptical responses that are several-orders-of-magnitude stronger than natural chiral materials. For example, for conventional chiral materials such as crystalline quartz, fluorite films, cholesteric liquid crystals, and chiral molecules, the typical values of optical chirality are smaller than 0.5 °/μm.[29] Such values have been increased to >40 °/μm in plasmonic chiral metamaterials.[69] The strongly enhanced chiroptical responses in chiral metamaterials have enabled ultrathin chiroptical devices. For example, gold helix chiral metamaterials with ¼ of the light wavelength in thickness can achieve near-unity transmission of incident CPL with opposite handedness while blocking CPL with the same handedness.[70] Moreover, the development of chiral metamaterials overcomes the wavelength limit in natural chiral molecules, which usually respond to the UV regime. Utilizing meta-atoms with different resonant wavelengths as building blocks, one can achieve chiral metamaterials for a wide range of wavelengths from UV to infrared.[38, 71, 72] Optical chirality in terahertz (THz) and gigahertz (GHz) regimes has also been achieved using metals with microwave resonances.[73, 74] The development of chiral metamaterials at different wavelength regimes has significantly expanded the capability to manipulate electromagnetic waves with circular polarization. Optical devices such as chiral polarizers, chiral photodetectors, and chiral meta-mirrors have been proposed and developed in recent years based on chiral metamaterials.[75-77] Tomita and co-workers have recently observed coupling between magnetic resonances and optical chirality in metamaterials, leading to strong optical magnetochiral effects, which are promising for one-way mirrors and synthetic gauge fields for electromagnetic wave.[78, 79] Besides far-field chiroptical responses, chiral metamaterials have enabled researchers to explore the strongly enhanced optical chirality in the near field, which is known as a superchiral field.[80] With the strongly confined light and localized electromagnetic hot spots, chiral metamaterials exhibit significantly enhanced chiral near fields, opening the pathway to utilizing the superchiral fields for applications in enantiodiscrimination, synthesis and sorting of chiral molecules.[80-84]

1.3 Chirality in moiré configurations

The development of chiral metamaterials relies on the generation of structural chirality or the breaking of spatial symmetry of light-matter interactions. A common strategy for chiral metamaterials is to design structures resembling natural chiral molecules and to replace the atoms with meta-atoms. For example, inspired by helical chirality in propellers and spiral molecules such as perchlorotripheylamine and helicenebisquinone, researchers have developed plasmonic or dielectric gammadions and spiral structures with strong chiroptical responses.[85] Analogous to coupled chiral molecules consisting of two or more achiral molecules, such as 2,2’-dimethoxy-binaphthyl, chiral metamaterials with coupled crosses, rods, and split rings have been achieved.[86-88] By stacking layers of chiral building blocks into 2D or 3D spiral structures, one can generate supramolecular chirality.[89] The helical structure of DNA molecules has also inspired the creation of metamaterials based on chiral scaffolds, including helically assembled Au nanoparticles, plasmonic gyroid networks, spiral thin films, and chiral nano-needles.[90-93] Optical chirality can also be observed when spatial symmetry is broken by introducing oblique incident light onto an achiral metasurface.[94] The chiral phenomenon without the existence of actual chiral entities is known as pseudochirality.[72]

Despite substantial progress in the past decade, chiral structures that break site-specific symmetry face challenges in fabrication and tunability. Time-consuming and costly fabrication techniques such as focused ion beam lithography, two-photon lithography, and electron beam lithography are often needed to achieve nanoscale building blocks in chiral metamaterials, especially those operating in the visible and infrared regimes. Such challenges have limited the applications of chiral metamaterials. Metamaterials based on pseudochirality have the advantage of simplicity in fabrication. However, the requirement for precisely controlled incident angles of light cannot be satisfied in many applications.

An alternative strategy to create chiral metamaterials is to transfer chirality from the macroscale to the nanoscale. This strategy is similar to supramolecular chirality but without the demand for chiral building blocks. For example, achiral nanoscale optical resonators can be assembled into macroscale structures that are twisted or rotated. The macroscale twist or rotation gives rise to structural chirality at the nanoscale, which therefore generates chiroptical responses. Kim et al. demonstrated reconfigurable chiroptical nanocomposites using this strategy.[95] They grafted achiral Au nanoparticles onto flexible elastic substrates to form uniform layers of plasmonic composites. The elastic substrates were twisted to generate macroscale structural chirality, which was transferred to the chirality in the nanoscale nanoparticle chains for a strong chiroptical response. Advantages of the transfer of chirality from macroscale to nanoscale include flexible tunability and potential for reconfigurability.

One of the most exciting directions for the control of nanoscale chiral features by macroscale manipulation is via moiré stacking, which typically refers to the superimposition of two identical or similar periodic lattices with translational or rotational displacement.[96, 97] Moiré stacking leads to visually fascinating moiré patterns, which have been widely used in applications such as optical alignment, document counterfeiting, and shearing strain analysis.[98-100] More details on moiré phenomena and moiré patterns are available in previous publications.[96, 97, 101]

Strong correlations between macroscale and nanoscale displacements can be obtained in moiré stacking due to the invariability of superimposing lattices. In other words, the nanoscale features can be predicted in structures generated by moiré stacking of two or more periodic lattices. Due to the strong correlation between macroscale and nanoscale features, moiré patterns have shown enormous value for developing optical metamaterials and metasurfaces. In recent years, a large amount of moiré metamaterials and metasurfaces have been developed by arranging plasmonic or photonic meta-atoms into moiré patterns, including plasmonic moiré superlattices, woodpile photonic crystals, and moiré graphene metasurfaces.[53, 102-104] The control over nanoscale features by macroscale manipulation in moiré stacking have made it possible to easily and precisely tune optical properties of moiré metamaterials by controlling relative lattice constants or rotation angles between two or more periodic arrays. Tunable moiré metamaterials and metasurfaces have thus been achieved by introducing moiré patterns in 2D arrays of gold or graphene nanostructures.[53, 54] The periodic lattices also enable high-throughput fabrication of moiré metamaterials and metasurfaces. For example, when the periodic lattices in superimposing layers are patterned using nanoimprint lithography, the wafer-scale moiré metamaterials and metasurfaces can be fabricated in a roll-to-roll manner.

Recently, moiré patterns have proved effective in transferring chirality from the macroscale to the nanoscale.[69, 105] 3D moiré stacking of two or more periodic lattices leads to prominent chiral structures. Figures 1a-c illustrate moiré stacking of one-dimensional (1D) gratings, 2D square-lattice arrays, and 2D triangular-lattice arrays, respectively. Different colors are used to depict the top (light) and bottom (dark) layers when viewed from above. An anticlockwise rotation of the bottom layer with respect to the top layer leads to LH structures, as shown in the left panels in Figures 1a-c, when the relative in-plane rotation angle (θ) is between 0 and π/R. R is the rotational symmetry of the lattices in superimposing layers, which is 2 for 1D gratings (Figures 1a), 4 for 2D square-lattice arrays (Figures 1b), and 6 for 2D triangular-lattice arrays (Figure 1c).[106] When the in-plane rotation of the bottom layer with respect to the top layer is -θ, as shown in the right 97panels in Figures 1a-c, moiré stacking leads to RH configurations. The schematics in Figure 1 show that the shaded area and rotational symmetry are the same in LH and RH moiré patterns. Therefore, when interacting with unpolarized or linearly polarized incident light, metamaterials with the moiré configurations do not have handedness-dependent optical responses. In these cases, the moiré configurations in Figure 1 have no structural chirality. In contrast, when the incident light has circular polarization, handedness-dependent light-matter interactions appear in the moiré metamaterials. In these cases, the moiré configurations in Figure 1 can be treated as 3D structures with the distinguishable layers depicted by different colors, leading to prominent structural chirality.

With tremendous progress in nanofabrication, periodic arrays of nanostructures like those in Figure 1 have been successfully fabricated with nanoscale precision and high throughput.[104-106] These moiré chiral metamaterials (MCMs) have attracted growing interests for both study of light-matter interactions at the nanoscale and engineering applications in various fields. In particular, the ease of control of nanoscale features and thus optical chirality by macroscale manipulation has made it possible to create reconfigurable chiral metamaterials by simply reconstructing chiral stacking between superimposing layers.[107]

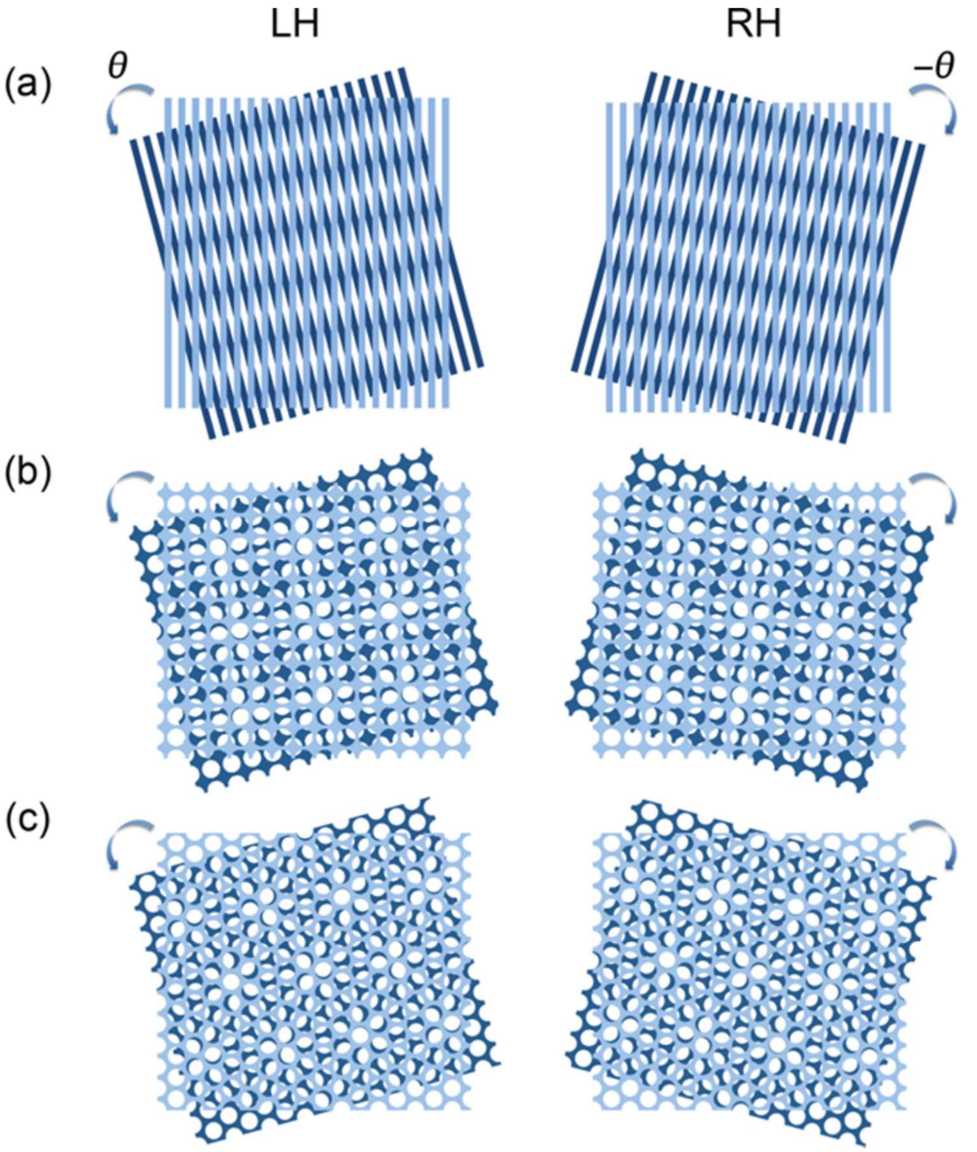

Figure 1. Handedness in moiré patterns. Schematics of moiré configurations with an opposite handedness formed by (a) 1D periodic grating, (b) 2D squared-lattices, and (c) 2D triangular-lattices, respectively. θ and $-\theta$ correspond to LH and RH structures, respectively.

In this Feature article, we review the recent progress in chiral metamaterials based on moiré stacking. After an introduction to the basics of optical chirality in metamaterials, we describe the physics of optical chirality and it tunability in moiré metamaterials. By comparing chiral metamaterials with different building blocks (i.e. particles, rods, and holes), we highlight that MCMs based on broken lattice-dependent symmetry feature advantages over conventional chiral metamaterials based on broken site-specific symmetry. Next, we discuss fabrication techniques toward chiral metamaterials with a focus on advantages of moiré stacking over conventional methods applied for chiral metamaterials that break site-specific symmetry. After that, we present the current applications of MCMs. We conclude with our perspectives on the future opportunities of MCMs.

2. Basics of optical chirality

When monochromatic electromagnetic radiation interacts with a molecule, it will become polarized and induce both electrical dipole moment and magnetic dipole moments:[85]

$$\tilde{\mathbf{p}} = \tilde{\alpha}\tilde{\mathbf{E}} - i\tilde{G}\tilde{\mathbf{B}}\ ,\ \ \tilde{\mathbf{m}} = \tilde{\chi}\tilde{\mathbf{B}} - i\tilde{G}\tilde{\mathbf{E}}\ , \tag{1}$$

where $\tilde{\alpha}$ is the electric polarizability with the value of $\tilde{\alpha} = \alpha' + i\alpha''$, $\tilde{\chi}$ is the magnetic susceptibility with the value of $\tilde{\chi} = \chi' + i\chi''$, $\tilde{G}$ is the isotropic mixed electric-magnetic dipole polarizability with the value of $\tilde{G} = G' + iG''$, $\tilde{\mathbf{E}}$ and $\tilde{\mathbf{B}}$ are time-dependent electrical and magnetic local field with the value of $\tilde{\mathbf{E}}(t) = \pm\widetilde{\mathbf{E_0}}e^{-iwt}$ and $\tilde{\mathbf{B}}(t) = \pm\widetilde{\mathbf{B_0}}e^{-iwt}$, respectively. The time-dependent absorption ($A^{\pm}$) of right-handed circularly polarized (RCP, +) and left-handed circularly polarized (LCP, -) incident light by the molecule can be obtained by:[108]

$$A^{\pm} = \langle \mathbf{E}\cdot\dot{\mathbf{p}} + \mathbf{B}\cdot\dot{\mathbf{m}}\rangle = \frac{\omega}{2}\left(\alpha''\left|\tilde{\mathbf{E}}\right|^2 + \chi''\left|\tilde{\mathbf{B}}\right|^2\right) \pm G''\omega\,\mathrm{Im}(\tilde{\mathbf{E}}^* \cdot \tilde{\mathbf{B}}) \tag{2}$$

The time-averaged electric and magnetic energy density are $U_e = \frac{\epsilon_o}{4}\left|\tilde{\mathbf{E}}\right|^2$ and $U_b = \frac{1}{4\mu_o}\left|\tilde{\mathbf{B}}\right|^2$, respectively. Thus, the time-averaged rate of absorption is stated as:

$$A^{\pm} = \frac{2}{\epsilon_o}\alpha''\omega(U_e + \gamma U_b) \mp \frac{2}{\epsilon_o}CG'' \tag{3}$$

where $\gamma = \frac{\chi''}{\alpha''}\epsilon_o\mu_o$. The absorption difference between RCP and LCP incident light arises from the second term $\frac{2}{\epsilon_o}CG''$ of Equation (3). Here, the C in $\frac{2}{\varepsilon_o}CG''$ is known as optical chirality, which determines the asymmetry in excitation rates between different chiral molecules:

$$C = -\frac{\varepsilon_o\omega}{2}\mathrm{Im}\left[\tilde{\mathbf{E}}^* \cdot \tilde{\mathbf{B}}\right] \tag{4}$$

By applying $\omega\mathrm{Im}\left[\tilde{\mathbf{E}}^* \cdot \tilde{\mathbf{B}}\right] = \dot{\mathbf{B}} \cdot \mathbf{E} - \dot{\mathbf{E}} \cdot \mathbf{B}$, the above equation can be expanded as:

$$C = \frac{1}{2}\left[\varepsilon_o\mathbf{E} \cdot \nabla \times \mathbf{E} + \frac{1}{\mu_o}\mathbf{B} \cdot \nabla \times \mathbf{B}\right] \tag{5}$$

The free space optical chirality for CPL is given by:

$$C_{CPL}^{\pm} = \pm\frac{\varepsilon_o\omega}{2c}|E|^2 \tag{6}$$

where c is the vacuum velocity of light. Thus, the relative local chirality enhancement is obtained by the ratio of $C^{\pm}$ and $C_{CPL}^{\pm}$, which is $\hat{C} = \frac{C^{\pm}}{|C|_{CPL}^{\pm}}$. Equation (6) indicates that the enhanced electric fields at chiral metamaterials increase the chirality and its associated light absorption, scattering and emission.

When CPL interacts with chiral metamaterials, the absorption difference between two circularly polarized lights (i.e., CD signal) can be greatly enhanced. For a chiral molecule near a chiral metamaterial, the molecule-metamaterial coupling will change the overall CD spectra. Considering a coupled molecule-plasmonic nanoparticle (NP) complex without the strong hybridization, one can split the enhanced CD signal into two parts:[109]

$$CD = CD_{molecules} + CD_{plasmon} \tag{7}$$

where $CD_{molecules}$ and $CD_{plasmon}$ are from the molecule and the NP, respectively, which contribute to two CD bands. For a molecular dipole, $CD_{molecules}$ can be calculated as:[110]

$$CD_{molecules} = E_o^2 \frac{8}{3}\sqrt{\varepsilon_o \omega_o}\frac{\Gamma}{|\hbar\omega-\hbar\omega_o+i\Gamma|^2} \times \mathrm{Im}\left[(\hat{P}\cdot\mu_{12})\cdot m_{21}\right] \tag{8}$$

where E_o is the magnitude of the local electrical field, Γ is the broadening and shift of the molecular resonance due to the interaction with the NP, ω_o is the frequency of the molecular resonance, the matrix $\hat{P}$ represents the NP induced optical electric field change inside the molecule, μ_{12} and m_{12} are the electric and magnetic transition dipole moments of the molecule, respectively. For a spherical plasmonic NP, $CD_{plasmon}$ can be expressed as:

$$CD_{plasmon} = \mathrm{Im}(\varepsilon_{NP})\frac{8}{9}\frac{a_{NP}^3}{\varepsilon_o R^3}E_o^2\sqrt{\varepsilon_o}\left|\frac{3\varepsilon_o}{(2\varepsilon_o+\varepsilon_{NP})}\right|^2 \times \mathrm{Im}\left[\frac{\mu_{12x}\cdot m_{21x}+\mu_{12y}\cdot m_{21y}+\mu_{12z}\cdot m_{21z}}{\hbar\omega-\hbar\omega_o+i\Gamma}\right] \tag{9}$$

where ε_{NP} is the dielectric constant of the NP, a_{NP} is the radius of the NP, R is the distance between the NP and the molecule, μ_{12i} and m_{21i} represents the electric and magnetic transition dipole moments of the molecule in *i* direction , respectively. As the NP-molecule distance increases, the CD signal decreases due to the reduced molecule-NP coupling. For a complex with n number of molecules and n number of NPs, the total *CD* is described as:

$$CD = \sum_{i=1}^{n} CD_{molecule,i} + \sum_{i=1}^{n} CD_{plasmon,i} \tag{10}$$

For a general large-scale chiral structure, the quasi-static approximation is no longer applicable. The long-range electromagnetic coupling method can be used to calculate the CD. In this case, Maxwell's equation and continuous model for chiral structures should be solved with position-dependent dielectric function[111, 112]:

$$D_\omega = \varepsilon E_\omega + i\xi_c B_\omega \tag{11}$$

$$H_\omega = \frac{B_\omega}{\mu} + i\xi_c E_\omega \tag{12}$$

where $\varepsilon(\omega, r)$ is position-dependent dielectric constant and $\xi_c(\omega, r)$ is the parameter describing the chiral property of the medium. This induces the effective refractive indices difference between RCP(+) and LCP(-) due to the structural chirality of the metamaterials:

$$n_{\pm} = \sqrt{\varepsilon\mu} \pm \chi \tag{13}$$

The difference in the imaginary part of the above equation gives the phase change for RCP and LCP light as they travel through the metamaterials, leading to a different extinction of RCP and LCP light.

Chiral metamaterials are also capable of manipulating linearly polarized light, which is an equal superposition of LCP and RCP light. Because RCP and LCP light have different refractive indices in chiral metamaterial, linearly polarized light travels through chiral metamaterials with its polarization rotated. Such phenomenon, which is known as optical rotatory dispersion (ORD), is characterized as:

$$\theta = \frac{(n_{+} - n_{-})\pi d}{\lambda_o} \tag{14}$$

where *d* is the thickness of the metamaterial, λ_o is the wavelength of light in vacuum, and n_+ and n_- are the effective refractive indices of RCP and LCP light, respectively.

An alternative parameter called dissymmetry factor *g* can also be used to evaluate the chiroptical response of the molecules, which is proportional to the absorption difference $A^{+} - A^{-}$ between RCP(+) and LCP(-) light normalized to the total absorption:

$$g = 2\frac{A^{+} - A^{-}}{A^{+} + A^{-}} \tag{15}$$

The contribution of the magnetic field is negligibly small in most cases. Therefore, the dissymmetry factor can be simplified as:

$$g = g_{CPL}\frac{cC}{2U_e\omega} \tag{16}$$

where $g_{CPL} = -4\frac{G"}{c\alpha"}$ is the dissymmetry factor in free space, *C* is the optical chirality, U_e is time-averaged electric energy density, $G"$ is the imaginary part of isotropic mixed electric-magnetic dipole polarizability. At the low electric energy density region, the magnetic energy cannot be considered negligible. Therefore, the full expression of *g* with the inclusion of magnetic energy density is:

$$g = g_{CPL}\frac{cC}{2(U_e+\gamma U_b)\omega} \tag{17}$$

where $\gamma = \frac{\chi''}{\alpha''}\epsilon_o\mu_o$, *C* is the optical chirality, U_e and U_b are time-averaged electric and magnetic energy density, respectively. This dimensionless factor ranges from -2 to +2, representing the magnitudes of CD signals. For typical organic molecules, the *g* value is normally small (~ 10^{-3}).[113] The dissymmetry value *g* can be enhanced by increasing the local optical chirality *C*, which has been demonstrated almost 11-fold chiroptical enhancement using superchiral fields.[82] In addition, *g* can also be increased by decreasing U_e or decreasing the local electrical field intensity.[47] Thus, a key factor in enhancing near-field (i.e. local chirality) and far-field (i.e. CD and ORD) chiroptical responses is large structural dissymmetry. In recent years, chiral metamaterials with large dissymmetry have been developed by breaking site-specific symmetry or lattice-dependent symmetry.

3. Optical chirality in chiral metamaterials and MCMs

In this section, we firstly discuss optical chirality in chiral metamaterials consisting of building blocks arranged in ways that break either site-specific symmetry or lattice-dependent symmetry. We highlight the advantages of breaking the lattice-dependent symmetry in MCMs. Next, we demonstrate tunable chiroptical coupling in MCMs. Finally, we discuss moiré chiral meta-films made by stacking atomically thin graphene layers.

3.1 Round-shaped particles as building blocks

Single round-shaped particles are achiral structures. Maoz et al.[110] demonstrated that, when a chiral molecule adsorbs onto an achiral silver NP, the NP surface plasmons can enhance the UV CD signal of the molecule. However, a single NP has limited chiroptical enhancement.[110, 114] By engineering the NPs into pairs, split-gate structures or nanoshells, Govorov et al. claimed that the optical coupling between the molecules and the engineered NP structures can amplify the natural CD signal of molecules through plasmonic concentration and enhancement of the electromagnetic fields at the small regions.[115] The coupling can also shift the CD signal of the molecules from the UV to the visible region. Still, the lack of structural asymmetry in achiral plasmonic structures has limited their chiroptical response. To further enhance chiroptical responses, multiple achiral NPs arranged into chiral structures have been explored.[116, 117] Banzer et al. studied a three-particle system in a chiral geometry.[118] As shown in Figure 2a, this heterotrimer exhibits material-composition asymmetry, leading to different absorption of RCP and LCP light. The asymmetric absorption behavior can be visualized by the constructive or destructive interference of near-field coupling within the trimers (Figure 2b).

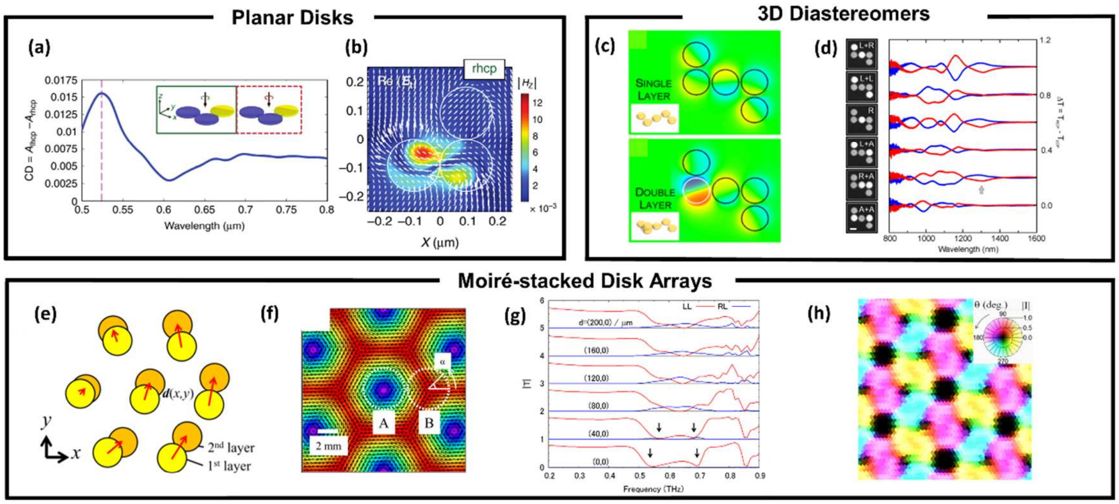

Figure 2. Round-shaped particles as building blocks. (a, b) Chiroptical response of a heterotrimer of planar disks: (a) Circular dichroism of the trimer system. The inset is the schematic of the disk trimer (blue is a silicon nanodisk; yellow is a gold nanodisk) under RCP and LCP light irradiation; (b) Field distributions at the trimer under 520 nm LCP light irradiation; (a, b) Reproduced with permission.[118] (c, d) Chiroptical responses of 3D gold diastereomers of nanodisks: (c) Simulated electric near-field distributions upon irradiation by LCP light for single- and double-layer assemblies; (d) Scanning electron micrographs and CD spectra of six different diastereomers; (c, d) Reproduced with permission.[119] (e-h) Chiroptical response of a moiré-stacked disk array: (e) Schematic of the moiré array with the displacement vectors *d(x, y)*; (f) Visualized displacement field of the moiré pattern over a large area; (g) Transmission spectra of LCP (blue) and RCP (red) light for different relative displacements; (h) Distributions of phase (indicated by color) and normalized intensity (indicated by brightness) on the moiré array; (e-h) Reproduced with permission.[120]

Hentschel et al. demonstrated that the chiroptical responses of planar chiral assembly of nanodisks can be tuned by adding an NP on the top of the assembly, as shown in Figure 2c.[119] This extra NP leads to a substantial increase in structural chirality, significantly enhancing the chiroptical responses and their tunability, as shown in Figure 2d.

Unlike the chiral assemblies of NPs in Figures 2a-d that break site-specific symmetry, moiré stacking leads to 3D structural chirality that breaks the lattice-dependent symmetry. For example, Ohno et al. created a 3D chiral metamaterial via moiré stacking of two layers of periodic disk arrays with lattice-dependent structural chirality. Strong optical chirality in such chiral metamaterials has been observed.[120] To better visualize the structural chirality, the displacement vector can be used to represent in-plane displacement from the center of a disk in the first layer to the center of the nearest disk within the second layer (Figure 2e,f). There is a strong circular displacement trajectory around the twisting center, which shows a periodic array of topological phase singularities. The relative displacement of the disk arrays alters the direction and magnitude of local circular trajectory and shifts the transmission spectra (Figure 2g), and the chiroptical response can also be characterized by the transmittance distribution at the resonant frequency. The 2D mapping in Figure 2h depicts the relative phase and intensity of the transmitted LCP light at a resonant frequency of 0.64 THz, where the topological singularities of the structure and the phase singularities near the surface match well with each other. This is a good demonstration of how the topological features of the moiré pattern are projected onto the electromagnetic field through a chiral metamaterial.

3.2 Rods as building blocks

Typical rod-built structures include single rods, C-shaped, L-shaped, Z-shaped, and even more complex rod arrangements.[121] Single rods and C-shaped rods are achiral structures due to their mirror symmetries. Therefore, these two types of rod-built structures show no optical chirality. However, the L- and Z-shaped rod assemblies are chiral (Figure 3a).[122-124] The Z-shaped assemblies can typically produce stronger optical rotation than the L-shaped structures because the additional short segment induces additional polarization (Figure 3b). For more complex chiral assemblies of rods such as gammadions, strong chiroptical responses have been found. Schaferling et al. showed that such a structure can produce >30-fold plasmonic enhancement of the optical rotation, though still an order of magnitude lower than that obtained with the L or Z rod assemblies.[85]

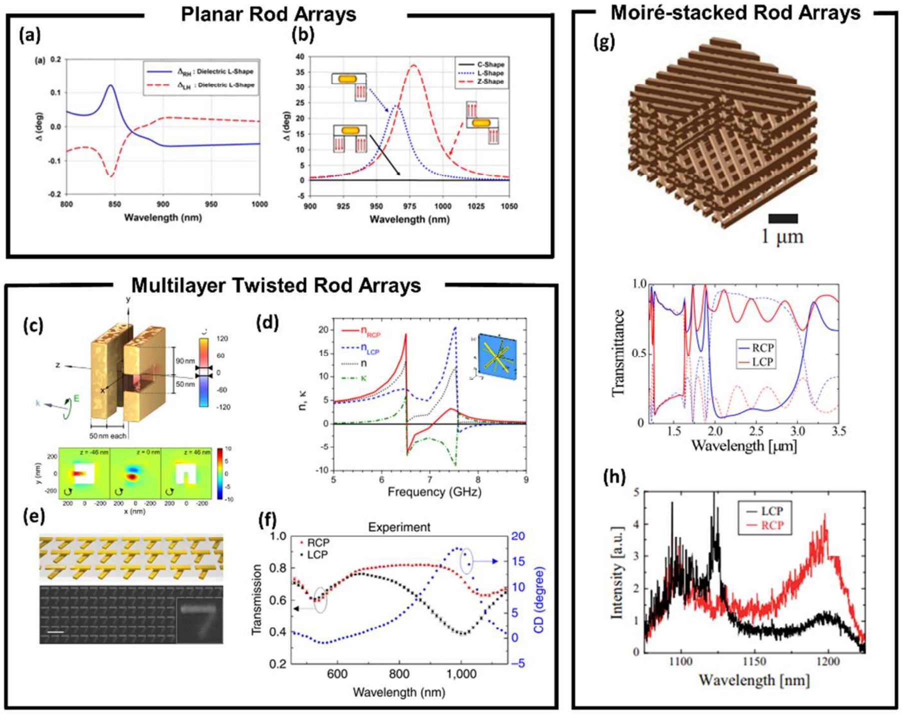

Figure 3. Rod arrays as building blocks. (a, b) Optical response of planar chiral-patterned dielectric metamolecules with an embedded achiral plasmonic nanostructure: (a) ORD spectra for an array of RH (solid blue line) and LH (dashed red line) dielectric L structures on a substrate; (b) Polarization rotation for L-, Z-, and C-shaped metamolecules with zero-degree polarization angle; (a, b) Reproduced with permission.[121] (c) Optical chirality enhancement induced by the twisted C-shaped structure under LCP light. (c) Reproduced with permission.[85] (d) The effective refractive index of the Au cross structure for RCP and LCP light. (d) Reproduced with permission.[125] (e, f) Optical chirality of twisted nanorod metamaterials: (e) Scanning electron micrograph and the corresponding illustration of a twisted nanorod system; (f) Experimentally measured transmission

of the twisted metamaterial with RCP and LCP light, and its extracted CD; (e, f) Reproduced with permission.[75, 126] (g, h) Optical chirality of 3D chiral photonic crystal: (g) Schematic of the 3D chiral photonic crystal, along with calculated transmittance spectra (solid lines) and reflectance spectra (dotted lines) for RCP (blue) and LCP (red) light; (h) PL spectra under LCP and RCP excitation for the chiral photonic crystal containing QDs; (g, h) Reproduced with permission.[127]

In an example where achiral building blocks can be used to build a chiral structure, strong optical chirality can be observed in bilayer C-shaped structures with site-specific twisting (Figure 3c).[88] The chiroptical response of such structures can be tuned both by the relative angle of the twisted C-shaped structures and the gap distance between two twisted-C structures.[85] Zhou et al. also demonstrated that bilayers of crossed wires can give giant CD with a negative refractive index (Figure 3d).[125] Here, the negative refractive index comes from the structural chirality rather than a negative index of the materials themselves. Zhao et al. fabricated twisted nanorod chiral metamaterials with a similar tunability based on the relative angle between anisotropic structures.[75, 126] Further study of the number of layers showed that, for a bilayer twisted nanorod arrays, one dominant response occurs due to the longitudinal surface plasmon resonance, while multilayer twisted nanorod metamaterials give broader chiroptical responses (Figures 3e and 3f). Here, the chiral mechanism can be analyzed through the dominant Floquet mode, which is significantly different from other strong coupling-induced extrinsic chirality between the neighboring pairs.

In comparison with site-specific symmetry breaking in rod-based chiral structures, lattice-dependent symmetry breaking can be achieved by moiré stacking of rod arrays, giving unique structural and chiroptical properties. Takahashi et al. demonstrated a semiconductor-based three-dimensional moiré chiral photonic crystal with three layers rotated by 60˚ forming a single helical unit with a broad chiroptical response (Figure 3g).[128] Two CD bands arising in these structures were shown to come from two different helical structures. The most selective transmission occurred at 1.3 μm, where the transmittance of RCP light was 85% and the transmittance of LCP light was 15%. This response could be tuned to different wavelength regions by scaling the crystal dimensions or changing the number of layers. These materials have potential for use as active chiral emitters by doping the quantum dots (QDs): A theoretical study of spontaneous emission from QDs embedded in 3D chiral photonic crystals demonstrated modulation of circular polarized light in vacuum, where the extinction ratio can reach 8 over the entire visible spectrum with only 390 nm total material thickness (Figure 3h).[129]

Stacked metallic nanostrips also show chiroptical responses with lattice-dependent symmetry breaking. Gao et al. fabricated two-layer gold gratings with strong chiroptical responses in the visible range.[130] The two predominant transmission dips correspond to the electric and magnetic resonances with parallel and anti-parallel current flowing on the top and bottom Au strips, respectively. Besides geometry-modulated CD spectra, chiroptical responses can also be tuned by the direction of incident light. Yun et al. demonstrated that ultra-thin helically stacked Al nanorods can provide non-resonant circular polarization of visible light.[131] Whether a dielectric photonic crystal or metallic nanostrips, the moiré stacking of multiple layers can lead to a higher excitation ratio than typical resonance-based structure and can give broader bandwidths due to collective surface plasmon effects.

3.3 Hole arrays as building blocks

It has been demonstrated that periodic nanohole arrays in metal films can have extraordinarily large transmission resonance due to the SPP (surface plasmon polariton)-mediated transmission and dynamic diffraction effects.[132, 133] Maoz et al. took advantage of this to show the chiral enhancement of nanohole arrays (Figure 4a).[94] Periodic nanohole arrays are achiral structures with normal incidence of light because the field pattern for two circular polarizations are exact mirror images and their difference cancels out. However, once the incident angle is tilted even slightly, a clear asymmetric CD response appears under two different circular polarizations (Figure 4b). An elliptical nanohole array penetrating through a metal/dielectric/metal film can also produce CD in the near infrared (NIR) region when the light is off-normal incidence.[134] With the metal film at the backside as a reflector, the metal/dielectric/metal structure can greatly enhance the CD absorption of the nanohole array under titled incident light. It also shows multiple broad CD bands, which arise from the coupling of internal and external SPP modes of different diffraction orders. To resolve the lack of CD response under normal-incident light, Rodrigues et al. stacked two elliptical nanohole arrays with site-dependent symmetry breaking, where the major axes of the ellipses were skewed by 22.5°, to achieve a linear chiroptical response of 0.58 and a maximum optical rotation of $2.3 \times 10^6\ °/cm$ (Figures 4c and 4d).[135]

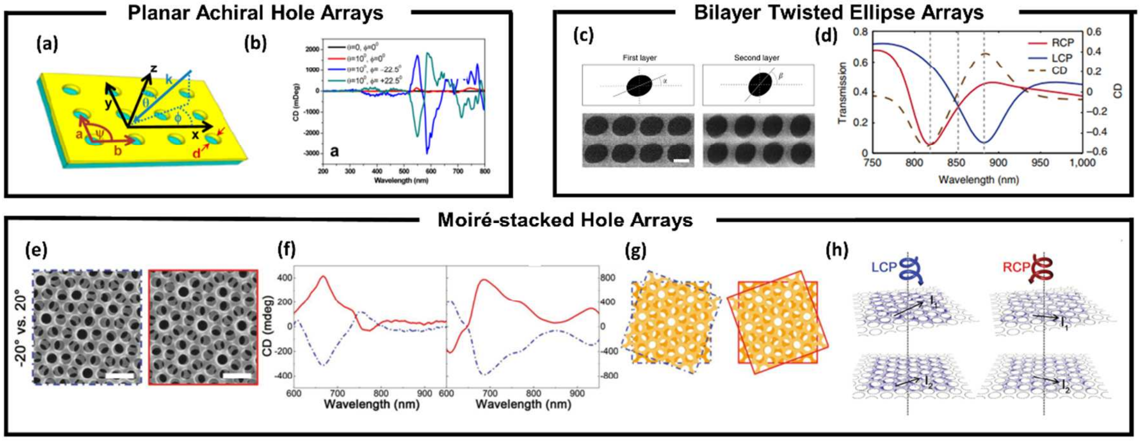

Figure 4. Nanohole-based chiral metamaterials. (a, b) Chiroptical effects in planar achiral nanohole: (a) Schematic of nanohole arrays; (b) Simulated CD spectra of nanohole arrays at several tilt angles; (a, b) Reproduced with permission.[94] (c, d) Stacked silver ellipses: (c) SEM images of ellipses in two layers; (d) Simulated transmission spectra of different CPL of the arrays

in (c); (c, d) Reproduced with permission.[135] (e-h) Chiroptical effects of MCMs: (e) SEM images, (f) measured and simulated CD spectra, and (g) schematic illustrations of MCMs; (h) Electron current distributions in the top and bottom layers of the MCM under LCP and RCP excitation; (e, f, g, h) Reproduced with permission.[105]

Site-dependent nanohole-based chiral metamaterials require precise alignment between the nanohole layers. We reported a new type of metamaterials called MCMs to eliminate the requirement for precise alignment. Briefly, MCMs can simply consist of two layers of identical nanohole arrays with periodic lattices stacked with an interlayer rotation angle, leading to lattice-dependent symmetry breaking.[105] The relative rotation angle of the two nanohole layers can be precisely tuned. Depending on the rotation angle, MCMs can be a RH or LH chiral structure, as shown in Figure 4e, which results in opposite handedness of optical responses near the plasmon resonance (Figures 4 f and 4g). To better understand the mechanism of chiroptical response, the light-induced effective current in both layers are simulated to show the different propagation directions under two polarizations (Figure 4h). The key feature of MCMs is the capability for tuning nanoscale optical chirality through macroscale manipulation. In other words, precise nanoscale lattice rotation of the MCMs can be achieved through macroscale mechanical rotation, which simplifies large-scale fabrication.

3.4 Tunable chiroptical coupling in MCMs

Lattice-dependent symmetry breaking in moiré chiral stacking has enabled exciting opportunities in achieving novel chiral metamaterials. One example is the utilization of propagating modes in plasmonic nanohole arrays and their coupling for tunable chiroptical activity. We demonstrated tunable and strong chiroptical coupling in MCMs by stacking two layers of identical Au nanohole arrays with a tunable dielectric spacer layer (Figure 5a).[69] The near-field coupling between the top and bottom layer not only dynamically tunes the spectral shift but can also increase the magnitude of the CD response (Figure 5b). The strongest optical chirality happens with an in-plane rotation angle of -15°/15° and a spacer thickness of ~25 nm. Modeling reveals that the tunability of MCMs arises mainly from gap surface plasmons (GSPs). However, the overall the spectral shape depends on near-field coupling between GSPs and SPPs, which leads to significant spatial differences in electrical hot-spot distribution under RCP and LCP light irradiation. As shown in Figure 5c, the large number of strong electrical hot spots in the spacer layer of 15° MCM indicates that strong GSPs are excited at a wavelength of 700 nm under RCP light. However, electrical hot spots are reduced in the spacer layer at a wavelength of 775 nm under RCP light. The polarization-dependent and spacer-dependent near-field coupling between GSPs and SPPs has led to strongly enhanced chiroptical responses that are tunable over 350 nm in wavelength.

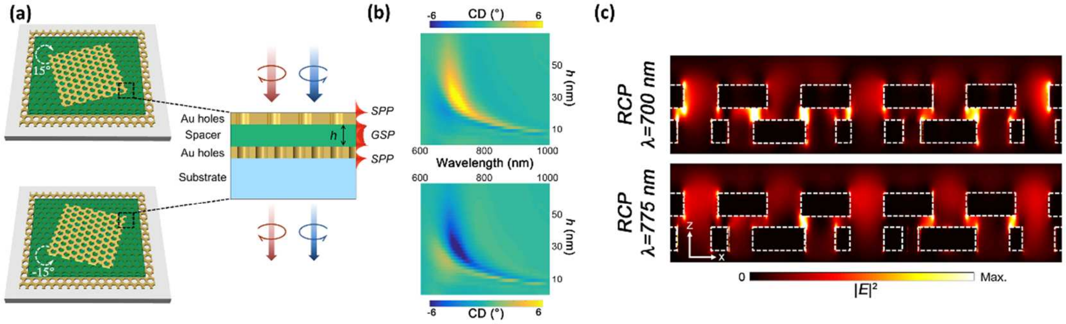

Figure 5. Tunable MCMs. (a) Schematic of RH (top panel) and LH (bottom panel) MCMs with relative in-plane rotation angles of 15° and −15°, respectively, along with cross-sectional view of the MCMs. (b) Simulated CD spectra of RH (top panel) and LH (bottom panel) MCMs as a function of spacer thickness. (c) Cross-sectional view of simulated electric intensity $|E|^2$ at 700 nm and 775 nm under RCP. Reproduced with permission.[69]

3.5 Moiré chiral meta-films of atomically thin materials

Moiré chiral stacking has further led to the development of tunable chiral meta-films based on atomically thin materials such as graphene, which is desirable for highly flexible and ultra-compact devices. Kim et al. reported a moiré stacking approach to achieving atomically thin chiral meta-films as shown in Figure 6a.[136] The chiral properties come from the large in-plane magnetic moment from graphene's interlayer optical transition. The incident light can introduce optical absorption for both achiral and chiral structures with a dynamic current (Figure 6b). However, a magnetic dipole moment can only be generated along with current in twisted graphene chiral materials while it disappears in achiral graphene. The coupling between the magnetic field of the light and the induced magnetic dipole moment in chiral materials can generate an additional chiral optical absorption, which leads to the absorption difference between two types of circular-polarized light (Figures 6c and 6d). Graphene-based tunable chiral meta-films can also be extended to other atomically thin materials such as transition metal dichalcogenides, allowing realization of versatile atomically thin chiral optical devices.

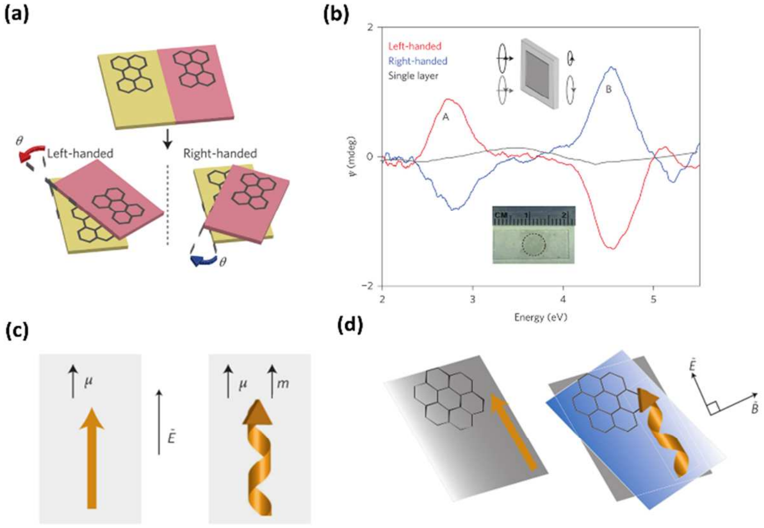

Figure 6. Tunable moiré chiral meta-films based on atomically thin materials. (a). Schematic of the chiral stacking process for generating LH and RH twisted bilayer graphene films. (b) CD spectra measured from a pair of chiral twisted bilayer graphene films. (c) An electric dipole μ is excited both in achiral (left panel) and chiral (right panel) materials. Only a magnetic moment m is excited in chiral (right panel) materials. (d) Different from single-layer graphene (left panel), interlayer optical transitions in moiré bilayer graphene can generate excited states delocalized

across both layers, which can host a helical current with an in-plane magnetic moment (right panel). Reproduced with permission.[136]

4. Fabrication techniques

Optical chiral materials consisting of different types of building blocks can be fabricated by various methods, including bottom-up, top-down and hybrid approaches. For small chiral structures such as nanoparticle-based chiral materials, precise manipulation tools such as atomic force microscopy are used to assembly the nanoparticles into the desired chiral geometry.[118, 137, 138] Methods such as DNA self-assembly can also be used to construct various types of chiral structures.[139] Here the DNA is predesigned as a chiral template with several vacant binding sites. By adding the plasmonic nanoparticles, DNA facilitates the binding of nanoparticle to these vacancies to form a chiral metamolecule. The chiroptical properties of the metamolecules can be actively controlled through modulating the dynamics of the DNA. As an example, Mastroianni et al. used DNA origami bundles to arrange attachment sites of 10 nm AuNPs into RH and LH chiral structures.[140] As shown in Figure 7a, the overall size of metamolecules can be as small as 30 nm, which is hard to achieve for traditional direct writing techniques.

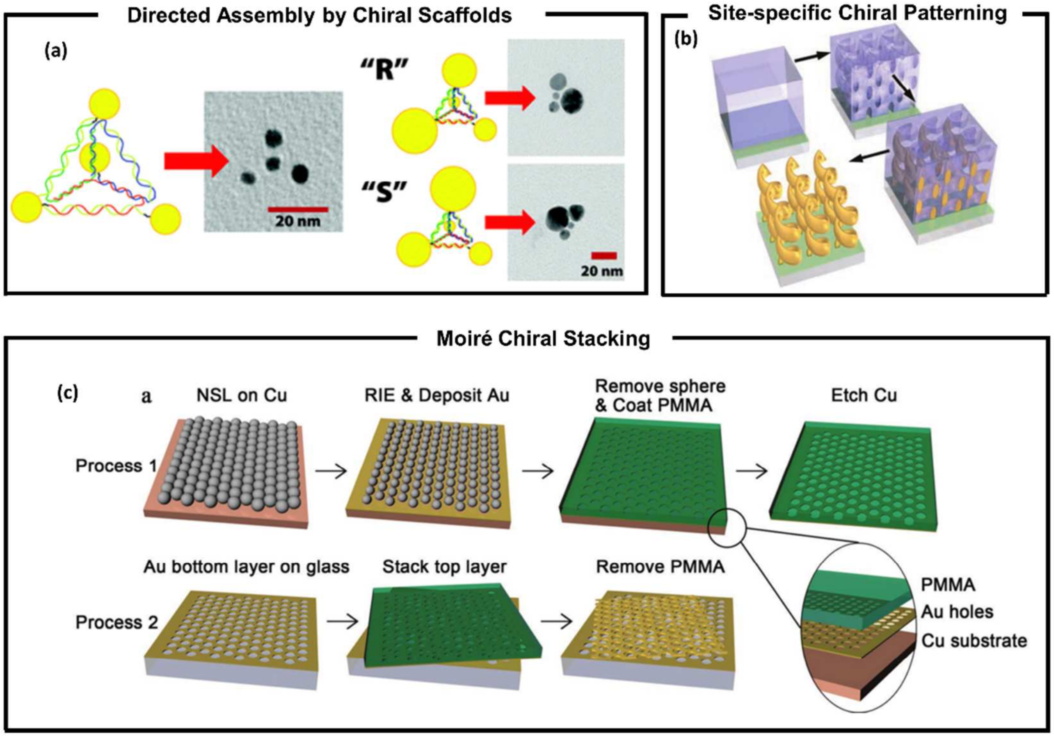

Figure 7. Fabrication of chiral metamaterials with nanoscale features. (a) Left- and right-handed nanohelices are formed by gold nanoparticles that are attached to the surface of DNA origami bundles. Reproduced with permission.[140] (b) Fabrication procedure of gold helix photonic metamaterials. Reproduced with permission.[70] (c) Fabrication procedure of MCMs. Reproduced with permission.[105]

To fabricate arrays of chiral structures with site-specific symmetry breaking in a top-down way, techniques such as electron-beam lithography, focused ion-beam-induced deposition and direct laser writing with multi-step alignments have been used. As an example, Gansel et al. fabricated gold helices using direct laser writing (Figure 7b).[70] Here, the polymer templates are first made via direct laser writing, and gold is then filled in the polymer templates by electrochemical deposition. In another large-area and low-cost chiral structure fabrication, Frank et al. showed that hole-mask lithography with tilted angle evaporation can fabricate chiral gold nanostructures over centimeters square.[141] The handedness of the spiral-like chiral structures can be dynamically tuned by the rotation direction of the sample holder during the evaporation.

In contrast to costly and time-consuming fabrication of chiral metamaterials based on the site-specific symmetry breaking, moiré stacking has reduced the constraints in fabrication and tunability. We have proposed a low-cost chiral structure fabrication procedure through moiré chiral stacking of plasmonic nanohole arrays fabricated by self-assembly of colloidal particles.[105] This fabrication includes two major processes, as shown in Figure 7c. Specifically, in the first process, Au nanohole arrays are created on a Cu substrate through traditional nanosphere lithography, followed by removal of the nanospheres and spin-coating a layer of PMMA. The Cu substrate is then selectively etched away and the floating thin film consists of the Au nanohole arrays and PMMA sacrificial layer. In the second process, nanosphere lithography is used to create Au nanohole arrays on a glass substrate. The two Au nanohole arrays from process 1 and process 2 are stacked together, leading to the MCMs with the two layers of Au nanohole arrays in contact. By tuning the evaporation or etching angle in nanosphere lithography, it is possible to achieve a variety of structures such as rings, stars, wires, and triangles.[142] The moiré stacking is broadly applicable to a variety of materials, including metal, dielectric, organic, and atomically thin materials.[143]

Another substantial advantage in fabrication of chiral metamaterials based on moiré stacking is the versatility in choosing functional materials as dielectric spacers. We have made use of this flexibility to achieve active chiral metamaterial with dynamic tunability by including silk fibroin as the dielectric spacer (Figure 8a).[69] The Au nanohole arrays were fabricated through a process similar to process 1 in Figure 7c. In process 2, instead of stacking the floating Au array on the Au bottom layer on the glass substrate, we spin-coated silk fibroin onto the bottom layer. The Au nanohole array layer from process 1 was then transferred onto the silk spacer to form an MCM with a silk interlayer. Active silk-MCMs were demonstrated by dynamically tuning the spacer thickness of the MCMs through silk expansion and shrinkage, which is controlled by the polarity of the solvents, as shown in Figure 8b.

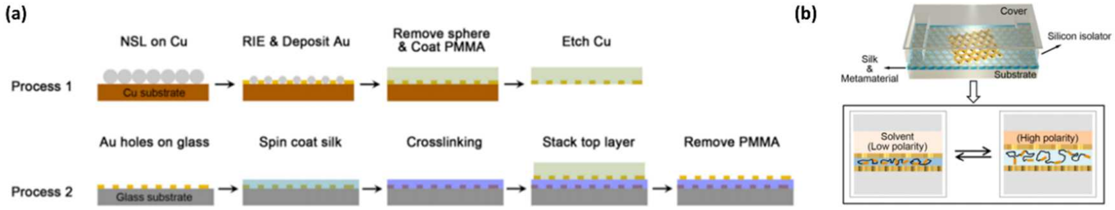

Figure 8. Fabrication of active MCMs. (a) Fabrication of active silk-MCMs. (b) A schematic of active silk-MCMs in response to solvents of low and high polarity. Reproduced with permission.[69]

Moiré stacking has also enabled controllable and tunable chiral meta-films at the wafer scale. As an initial demonstration, Kim et al. demonstrated the precise control of chiroptical responses of graphene chiral meta-films by tuning the interlayer angle of two spatially uniform graphene layers.[136] The fabrication process is shown in Figure 9. Multilayer moiré graphene can also be achieved by repeating the above procedure for multiple times. Benefiting from the macroscale to nanoscale chirality transfer in moiré chiral stacking, centimeter-scale spatially uniform chiral meta-films with precisely controllable structural and optical chirality have been achieved.

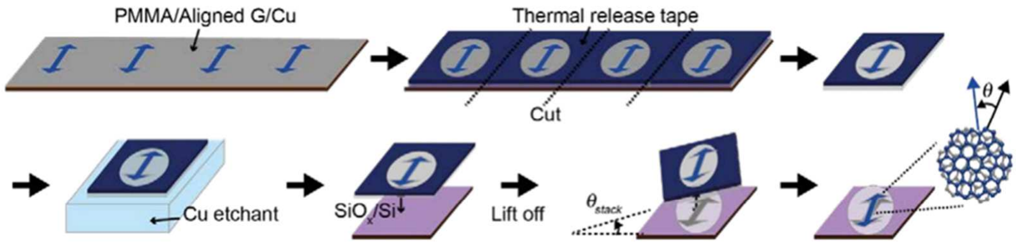

Figure 9. Fabrication of bilayer moiré chiral meta-films with precisely controllable chirality. The graphene was grown on a Cu sacrificial layer. The thermal release tape was attached onto the graphene surface. After selectively etching away the Cu layer, the thermal release tape with graphene was transferred to a SiO_x/Si substrate. The offset angle of bilayer moiré graphene was controlled by the relative angle between the edges of the two thermal release tapes. Reproduced with permission.[136]

5. Applications

A variety of applications based on MCMs have been demonstrated and proposed in recent years. As examples, we discuss the uses of MCMs in sensors and reconfigurable devices.

5.1 Biomedical sensors

It has been demonstrated that superchiral fields at chiral metamaterials can largely enhance the enantioselective excitation of chiral molecules.[144, 145] Plasmonic chiral metasurfaces have been applied to detect structural chirality of biological molecules such as concanavalin A, bovine serum albumin, and shikimate kinase at picogram quantities.[83, 144, 145] Such a strategy provides a label-free and ultrasensitive method to discriminate between enantiomers, which has significant implications in drug safety and medical applications. Nowadays, more than 55% of the current drugs, including commonly used ones like ibuprofen and ofloxacin, are chiral substances.[146]

Although they share the same chemical makeup, most enantiomers of chiral drugs have large differences in biomedical activities, including metabolism, toxicology, and pharmacology. In many cases, including the infamous thalidomide example, the safe and pharmacologically-active chiral drugs have “evil twins” that are harmful to human body. In 2015, 19 out of the 20 new chiral drugs approved by the US Food and Drug Administration have been required to be enantiomerically pure.[147] However, due to the weak intrinsic chiroptical responses of drug molecules, chiral sensing often requires tedious sample preparation, large amounts of sample, and long measurement times, hindering the drug development.

Recently, we have demonstrated that the strong superchiral fields in MCMs can be applied for surface-enhanced enantiodiscrimination of chiral drug molecules.[105] The sensing was based on plasmon-enhanced polarimetry, which detects the structural chirality of molecules by comparing the difference in spectral shift of plasmonic chiral metamaterials upon the adsorption of LH or RH molecules. The adsorption of molecules on the surface of MCMs induced spectral shifts of CD peak/dip ($\Delta\lambda$) due to changes in the dielectric environment (Figure 10a). The value of $\Delta\lambda$ was dependent on the relative chirality between the MCMs and the adsorbed molecules, where chiral molecules caused asymmetric spectral shifts of LH ($\Delta\lambda_L$) and RH ($\Delta\lambda_R$) MCMs. The asymmetry in spectral shift ($\Delta\Delta\lambda$) can be used to characterize the chirality of the bound molecules. We observed a significant $\Delta\Delta\lambda$ in LH and RH MCMs caused by the adsorption of concanavalin A, where achiral molecules had a negligible effect (Figure 10a). We have further applied the MCMs to detect the stereochemistry of small drug molecules (Figure 10b). The enhanced and localized superchiral fields enabled the enantioselective discrimination of a therapeutic chiral drug “R-thalidomide” from its toxic enantiomer, “L-thalidomide”, as demonstrated by the opposite signs in $\Delta\Delta\lambda$.

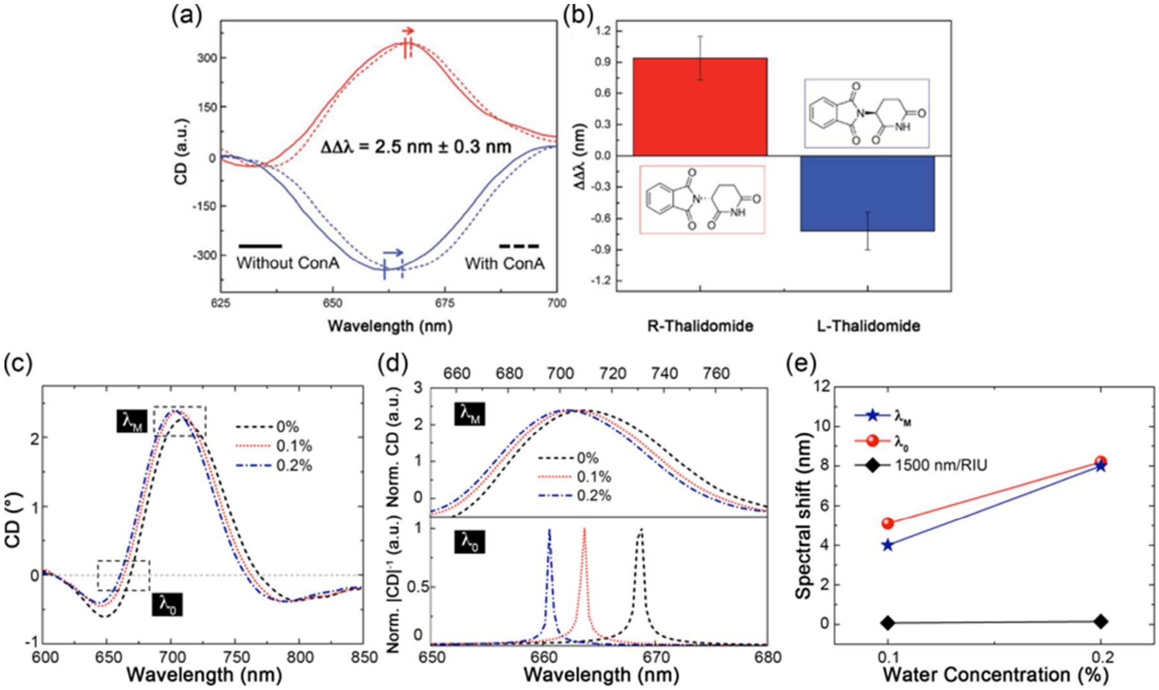

Figure 10. Applications of MCMs. (a, b) Enantiodiscrimination of chiral molecules based on MCMs: (a) CD spectra of the LH (blue) and RH (red) MCMs with (solid) and without (dashed) the adsorption of Concanavalin A (ConA); (b) asymmetric spectral shift (ΔΔλ) induced by R-thalidomide and L-thalidomide. (a, b) Reproduced with permission.[105] (c-e) Ultrasensitive detection of water contaminants in isopropyl alcohol (IPA) based on silk-MCMs: (c) CD spectra of a silk-MCM exposed to water-IPA mixtures with different concentrations of water; (d) (Top panel) Normalized CD spectra around the wavelength of λ_M as indicated by a dashed square in (c); (Bottom panel) Normalized $|CD|^{-1}$ spectra around the wavelength of λ_0, as indicated by a dashed square in (c); (e) Spectral shifts of λ_M and λ_0 with the inclusion of water in IPA with different concentrations. The spectral shift of a state-of-the-art refractive index sensor with sensitivity of 1500 nm/refractive index units (RIU) is shown for comparison. (c-e) Reproduced with permission.[69] The high sensitivity and figure of merit of silk-MCM in detecting solvent contaminants are promising in oil industry, chemistry, and high-precision machinery, where high-polarity contaminants such as water should be eliminated to avoid degradation of devices.[69]

5.2 Chemical sensors

The bipolar signatures in CD spectra offer an effective way to reduce the spectral linewidth, leading to a high figure of merit when applying chiral plasmonic structures for refractive index sensing.[148] As an example, we have demonstrated ultrasensitive detection of solvent contamination using MCMs with silk fibroin as dielectric spacer.[69] The volume of silk fibroin is highly sensitive to the polarity of the surrounding medium. Therefore, a small increase in the solvent polarity can lead to substantial expansion in the spacer thickness and thus a large spectral shift in the CD spectrum of the MCM. As an initial demonstration, we have applied the silk-MCMs to detect trace amounts of water in isopropyl alcohol (IPA), where 0.1% of water in IPA led to an obvious spectral shift in the CD spectra of the silk-MCM, resulting in a sensitivity of ~1 x 10^5 nm/RIU (Figures 10c-e). The bipolar shape of the CD spectrum further enables quantitative analyses of the water impurity by the normalization of the $|CD|^{-1}$ spectrum around the wavelength of the zero-crossing point in the CD spectrum, as denoted by λ_0 in Figure 10c. The ultrasensitive detection of methanol in hexane has also been demonstrated in a similar way with a sensitivity of 0.02% (v/v) (i.e. 200 ppm) and even below.

5.3 Reconfigurable devices

Reconfigurable metamaterials and devices can improve the optical tunability and operating bandwidth for enhanced applications.[149, 150] The reconfigurability in optical chirality has shown potential in a variety of applications, including information storage, communication, and display.[38] The MCMs enable the reconfigurable devices based on the change of the structural chirality in a precisely controllable way. Han et al. demonstrated a rotationally reconfigurable metamaterial based on moiré stacking of periodic metallic discs with square-lattice arrays, where reversible binding between the two layers allowed tunable moiré patterns.[107] Benefiting from the predictable features by the interlayer rotation in moiré patterns, both the number and amplitude of resonance bands can be precisely tuned and reconfigured, leading to tunable filters and modulators.

6. Summary and Perspectives

The transfer of chirality from macroscale to nanoscale through moiré stacking is promising to create chiral metamaterials from a variety of building blocks. The versatile tuning of moiré patterns and structural chirality arises from the variable numbers of superimposing layers and interlayer displacements. The spacer layers in the MCMs further enable the strong chiroptical coupling and response with flexible tunability for the enhanced applications. For example, by using suitable dielectric spacers in the MCMs that can change volumes in response to targeted analytes, one can achieve the sensors for various molecular detection. Ultrasensitive heat or light detectors can also be developed by using thermo- or light-responsive polymers as the spacer layers.

MCMs are highly compatible with the large-scale nanomanufacturing techniques. For example, we are applying roll-to-roll nanoimprint lithography to achieve large-scale high-throughput fabrication of the MCMs. With their cost-effective large-scale fabrication, strong chiroptical responses and high reconfigurability, MCMs will find a wider range of applications in various fields.

So far, most of the reported MCMs have been two-layer structures. The effects of increasing numbers of superimposing layers on the chiroptical properties remain to be investigated. To move forward, one would expect to observe new phenomena from the MCMs where chiral features or nonperiodic lattices were included in the individual layers. Nonlinear chiroptical effects in MCMs have yet to be explored. The study of nonlinear effects such as second and third harmonic generation, chiral-dependent two-photon optical processes, and magneto-chiroptics in the MCMs would lead to exciting new physics and applications.

Acknowledgements

The authors acknowledge the financial support of the Office of Naval Research Young Investigator Program (N00014-17-1-2424) and the National Aeronautics and Space Administration Early Career Faculty Award (80NSSC17K0520).

Conflict of Interest

The authors declare no competing financial interest.

References

1. W. T. B. Kelvin, *The molecular tactics of a crystal*, Clarendon Press, 1894.
2. L. A. Nguyen, H. He and C. Pham-Huy, *International journal of biomedical science: IJBS*, 2006, **2**, 85.
3. C. Deutsche, D. Lightner, R. W. Woody and A. Moscowitz, *Annual Review of Physical Chemistry*, 1969, **20**, 407-448.
4. J. Parnell, D. Cullen, M. R. Sims, S. Bowden, C. S. Cockell, R. Court, P. Ehrenfreund, F. Gaubert, W. Grant, V. Parro, M. Rohmer, M. Sephton, H. Stan-Lotter, A. Steele, J. Toporski and J. Vago, *Astrobiology*, 2007, **7**, 578-604.
5. R. Shapiro and D. Schulze-Makuch, *Astrobiology*, 2009, **9**, 335-343.
6. R. L. Crawford, A. Paszczynski, Q. Lang, I. F. Cheng, B. Barnes, T. J. Anderson, R. Wells, C. Wai, G. Corti, L. Allenbach, D. P. Erwin, J. Park, T. Assefi and M. Mojarradi, *Icarus*, 2001, **154**, 531-539.
7. B. A. McGuire, P. B. Carroll, R. A. Loomis, I. A. Finneran, P. R. Jewell, A. J. Remijan and G. A. Blake, *Science*, 2016, **352**, 1449-1452.

8. G. D'Orazio, C. Fanali, M. Asensio-Ramos and S. Fanali, *TrAC Trends in Analytical Chemistry*, 2017, **96**, 151-171.
9. M. Pasteur, *Ann. Chim. Phys.*, 1848, **24**, 442.
10. J. Bailey, *Origins of life and evolution of the biosphere*, 2001, **31**, 167-183.
11. A. Jorissen and C. Cerf, *Origins of life and evolution of the biosphere*, 2002, **32**, 129-142.
12. V. Sharma, M. Crne, J. O. Park and M. Srinivasarao, *Science*, 2009, **325**, 449-451.
13. A. C. Neville and B. M. Luke, *Journal of Insect Physiology*, 1971, **17**, 519-526.
14. R. Hegedüs, G. Szél and G. Horváth, *Vision Research*, 2006, **46**, 2786-2797.
15. A. A. Michelson, *The London, Edinburgh, and Dublin Philosophical Magazine and Journal of Science*, 1911, **21**, 554-567.
16. D. B. Shapiro, A. J. Hunt, M. S. Quinby-Hunt and P. G. Hull, 1991.
17. A. Gafni, H. Hardt, J. Schlessinger and I. Z. Steinberg, *Biochimica et Biophysica Acta (BBA) - Bioenergetics*, 1975, **387**, 256-264.
18. H. Wynberg, E. W. Meijer, J. C. Hummelen, H. P. J. M. Dekkers, P. H. Schippers and A. D. Carlson, *Nature*, 1980, **286**, 641.
19. W. C. Johnson Jr, *Annual review of biophysics and biophysical chemistry*, 1988, **17**, 145-166.
20. O. McConnell, A. Bach, C. Balibar, N. Byrne, Y. Cai, G. Carter, M. Chlenov, L. Di, K. Fan, I. Goljer, Y. He, D. Herold, M. Kagan, E. Kerns, F. Koehn, C. Kraml, V. Marathias, B. Marquez, L. McDonald, L. Nogle, C. Petucci, G. Schlingmann, G. Tawa, M. Tischler, R. T. Williamson, A. Sutherland, W. Watts, M. Young, M.-Y. Zhang, Y. Zhang, D. Zhou and D. Ho, *Chirality*, 2007, **19**, 658-682.
21. X. Wu, L. Xu, L. Liu, W. Ma, H. Yin, H. Kuang, L. Wang, C. Xu and N. A. Kotov, *J Am Chem Soc*, 2013, **135**, 18629-18636.
22. W. Ma, H. Kuang, L. Xu, L. Ding, C. Xu, L. Wang and N. A. Kotov, *Nature Communications*, 2013, **4**, 2689.
23. Z. Hasan, J. Jeon and S. H. Jhung, *J Hazard Mater*, 2012, **209-210**, 151-157.
24. I. J. Hodgkinson, Q. Wu, K. E. Thorn and M. D. Arnold, 2000.
25. Q. Wu, I. J. Hodgkinson and A. Lakhtakia, 2000.
26. I. J. Hodgkinson, A. Lakhtakia and Q. Wu, 2000.
27. I. J. Hodgkinson, Q. h. Wu, A. Lakhtakia and M. W. McCall, *Optics Communications*, 2000, **177**, 79-84.
28. I. J. Hodgkinson, Q. H. Wu, K. E. Thorn, A. Lakhtakia and M. W. McCall, *Optics Communications*, 2000, **184**, 57-66.
29. I. Hodgkinson and Q. h. Wu, *Advanced materials*, 2001, **13**, 889-897.
30. G. P. Nordin, J. T. Meier, P. C. Deguzman and M. W. Jones, *JOSA A*, 1999, **16**, 1168-1174.
31. M. Liu, L. Zhang and T. Wang, *Chemical reviews*, 2015, **115**, 7304-7397.
32. V. K. Valev, J. J. Baumberg, C. Sibilia and T. Verbiest, *Advanced Materials*, 2013, **25**, 2517-2534.
33. A. V. Zayats, I. I. Smolyaninov and A. A. Maradudin, *Physics Reports*, 2005, **408**, 131-314.
34. L. Zhang, S. Mei, K. Huang and C.-W. Qiu, *Advanced Optical Materials*, 2016, **4**, 818.
35. N. Yu and F. Capasso, *Nature Materials*, 2014, **13**, 139-150.
36. A. F. Koenderink, A. Alù and A. Polman, *Science*, 2015, **348**, 516-521.
37. N. Meinzer, W. L. Barnes and I. R. Hooper, *Nature Photonics*, 2014, **8**, 889-898.
38. J. T. Collins, C. Kuppe, D. C. Hooper, C. Sibilia, M. Centini and V. K. Valev, *Advanced Optical Materials*, 2017, **5**, 1700182.
39. J. A. Schuller, E. S. Barnard, W. Cai, Y. C. Jun, J. S. White and M. L. Brongersma, *Nature materials*, 2010, **9**, 193.

40. S. V. Boriskina, H. Ghasemi and G. Chen, *Materials Today*, 2013, **16**, 375-386.
41. Z. Wu, Z. Wang, S. Wang and Z. Zhong, *Nanoscale Research Letters*, 2014, **9**, 495.
42. R. Verre, L. Shao, N. Odebo Lank, P. Karpinski, A. B. Yankovich, T. J. Antosiewicz, E. Olsson and M. Kall, *Advanced Materials*, 2017, **29**, 1701352.
43. E. S. Goerlitzer, R. N. Klupp Taylor and N. Vogel, *Advanced Materials*, 2018, 1706654.
44. J. E. G. J. Wijnhoven and W. L. Vos, *Science*, 1998, **281**, 802-804.
45. Z. Wu, H. Lei, T. Zhou, Y. Fan and Z. Zhong, *Nanotechnology*, 2014, **25**, 055204.
46. A. I. Kuznetsov, A. E. Miroshnichenko, M. L. Brongersma, Y. S. Kivshar and B. Luk'yanchuk, *Science*, 2016, **354**.
47. C.-S. Ho, A. Garcia-Etxarri, Y. Zhao and J. Dionne, *ACS Photonics*, 2017, **4**, 197-203.
48. N. Liu, M. Mesch, T. Weiss, M. Hentschel and H. Giessen, *Nano letters*, 2010, **10**, 2342-2348.
49. H.-T. Chen, *Opt. Express*, 2012, **20**, 7165-7172.
50. K. Chen, R. Adato and H. Altug, *ACS Nano*, 2012, **6**, 7998-8006.
51. Z. Wu, W. Li, M. N. Yogeesh, S. Jung, A. L. Lee, K. McNicholas, A. Briggs, S. R. Bank, M. A. Belkin and D. Akinwande, *Advanced Optical Materials*, 2016, **4**, 2035-2043.
52. Z. Wu, K. Chen, R. Menz, T. Nagao and Y. Zheng, *Nanoscale*, 2015, **7**, 20391-20396.
53. Z. Wu, G. Kelp, M. N. Yogeesh, W. Li, K. M. McNicholas, A. Briggs, B. B. Rajeeva, D. Akinwande, S. R. Bank, G. Shvets and Y. Zheng, *Nanoscale*, 2016, **8**, 18461-18468.
54. Z. Wu and Y. Zheng, *Plasmonics*, 2015, **11**, 1-10.
55. W. Cai, U. K. Chettiar, A. V. Kildishev and V. M. Shalaev, *Nat Photon*, 2007, **1**, 224-227.
56. C. M. Soukoulis and M. Wegener, *Nature Photonics*, 2011, **5**, 523.
57. J. Yao, Z. Liu, Y. Liu, Y. Wang, C. Sun, G. Bartal, A. M. Stacy and X. Zhang, *Science*, 2008, **321**, 930.
58. X. Ni, Z. J. Wong, M. Mrejen, Y. Wang and X. Zhang, *Science*, 2015, **349**, 1310-1314.
59. J. F. Galisteo-Lopez, M. Ibisate, R. Sapienza, L. S. Froufe-Perez, A. Blanco and C. Lopez, *Adv Mater*, 2011, **23**, 30-69.
60. N. Vogel, M. Retsch, C. A. Fustin, A. Del Campo and U. Jonas, *Chemical Reviews*, 2015, **115**, 6265-6311.
61. C. Zhao, Y. Liu, Y. Zhao, N. Fang and T. J. Huang, *Nature Communications* 2013, **4**, 2305.
62. C. Ma and Z. Liu, *Opt. Express*, 2012, **20**, 2581-2586.
63. Y. Zhao, S.-C. S. Lin, A. A. Nawaz, B. Kiraly, Q. Hao, Y. Liu and T. J. Huang, *Opt. Express*, 2010, **18**, 23458-23465.
64. L. Maigyte, V. Purlys, J. Trull, M. Peckus, C. Cojocaru, D. Gailevičius, M. Malinauskas and K. Staliunas, *Optics letters*, 2013, **38**, 2376-2378.
65. D. Lin, Z. Wu, S. Li, W. Zhao, C. Ma, J. Wang, Z. Jiang, Z. Zhong, Y. Zheng and X. Yang, *ACS Nano*, 2017, **11**, 1478-1487.
66. L. Lin and Y. Zheng, *Nanoscale*, 2015, **7**, 12205-12214.
67. V. Flauraud, T. S. van Zanten, M. Mivelle, C. Manzo, M. F. Garcia Parajo and J. Brugger, *Nano Lett.*, 2015, **15**, 4176-4182.
68. C. Wu, A. B. Khanikaev, R. Adato, N. Arju, A. A. Yanik, H. Altug and G. Shvets, *Nat Mater*, 2012, **11**, 69-75.
69. Z. Wu, X. Chen, M. Wang, J. Dong and Y. Zheng, *ACS Nano*, 2018, **12**, 5030-5041.
70. J. K. Gansel, M. Thiel, M. S. Rill, M. Decker, K. Bade, V. Saile, G. von Freymann, S. Linden and M. Wegener, *Science*, 2009, **325**, 1513-1515.
71. A. Guerrero-Martínez, J. L. Alonso-Gómez, B. Auguié, M. M. Cid and L. M. Liz-Marzán, *Nano Today*, 2011, **6**, 381-400.

72. V. K. Valev, J. J. Baumberg, C. Sibilia and T. Verbiest, *Advanced Materials*, 2013, **25**, 2517-2534.
73. M. Kenney, S. Li, X. Zhang, X. Su, T. T. Kim, D. Wang, D. Wu, C. Ouyang, J. Han and W. Zhang, *Advanced Materials*, 2016, **28**, 9567-9572.
74. M. Liu, D. A. Powell, I. V. Shadrivov and Y. S. Kivshar, *Applied Physics Letters*, 2012, **100**, 111114.
75. Y. Zhao, M. A. Belkin and A. Alu, *Nature Communications*, 2012, **3**, 870.
76. Z. Wang, H. Jia, K. Yao, W. Cai, H. Chen and Y. Liu, *ACS Photonics*, 2016, **3**, 2096-2101.
77. W. Li, Z. J. Coppens, L. V. Besteiro, W. Wang, A. O. Govorov and J. Valentine, *Nature Communications*, 2015, **6**, 8379.
78. S. Tomita, K. Sawada, A. Porokhnyuk and T. Ueda, *Physical review letters*, 2014, **113**, 235501.
79. S. Tomita, H. Kurosawa, T. Ueda and K. Sawada, *Journal of Physics D: Applied Physics*, 2018, **51**, 083001.
80. Y. Tang and A. E. Cohen, *Science*, 2011, **332**, 333-336.
81. N. Yang and A. E. Cohen, *J Phys Chem B*, 2011, **115**, 5304-5311.
82. Y. Tang and A. E. Cohen, *Phys Rev Lett*, 2010, **104**, 163901.
83. E. Hendry, T. Carpy, J. Johnston, M. Popland, R. V. Mikhaylovskiy, A. J. Lapthorn, S. M. Kelly, L. D. Barron, N. Gadegaard and M. Kadodwala, *Nature Nanotechnology*, 2010, **5**, 783-787.
84. Y. Zhao, A. A. E. Saleh and J. A. Dionne, *ACS Photonics*, 2016, **3**, 304-309.
85. M. Schäferling, D. Dregely, M. Hentschel and H. Giessen, *Physical Review X*, 2012, **2**, 031010.
86. M. J. Huttunen, G. Bautista, M. Decker, S. Linden, M. Wegener and M. Kauranen, *Opt. Mater. Express*, 2011, **1**, 46-56.
87. Y. Tang, L. Sun and A. E. Cohen, *Applied Physics Letters*, 2013, **102**, 043103.
88. N. Liu, H. Liu, S. Zhu and H. Giessen, *Nature Photonics*, 2009, **3**, 157-162.
89. M. Decker, R. Zhao, C. M. Soukoulis, S. Linden and M. Wegener, *Optics Letters*, 2010, **35**, 1593-1595.
90. S. Vignolini, N. A. Yufa, P. S. Cunha, S. Guldin, I. Rushkin, M. Stefik, K. Hur, U. Wiesner, J. J. Baumberg and U. Steiner, *Advanced Materials*, 2012, **24**, OP23-27.
91. A. Kuzyk, R. Schreiber, Z. Fan, G. Pardatscher, E.-M. Roller, A. Högele, F. C. Simmel, A. O. Govorov and T. Liedl, *Nature*, 2012, **483**, 311-314.
92. K. Toyoda, K. Miyamoto, N. Aoki, R. Morita and T. Omatsu, *Nano letters*, 2012, **12**, 3645-3649.
93. D. Barada, G. Juman, I. Yoshida, K. Miyamoto, S. Kawata, S. Ohno and T. Omatsu, *Applied Physics Letters*, 2016, **108**, 051108.
94. B. M. Maoz, A. B. Moshe, D. Vestler, O. Bar-Elli and G. Markovich, *Nano letters*, 2012, **12**, 2357-2361.
95. Y. Kim, B. Yeom, O. Arteaga, S. Jo Yoo, S. G. Lee, J. G. Kim and N. A. Kotov, *Nature Materials*, 2016, **15**, 461-468.
96. V. G. Achanta, *Progress in Quantum Electronics*, 2015, **39**, 1-23.
97. G. Oster, M. Wasserman and C. Zwerling, *JOSA*, 1964, **54**, 169-175.
98. N. Li, W. Wu and S. Y. Chou, *Nano letters*, 2006, **6**, 2626-2629.
99. V. J. Cadarso, S. Chosson, K. Sidler, R. D. Hersch and J. Brugger, *Light: Science and Applications*, 2013, **2**, e86.
100. F.-P. Chiang, *Experimental Mechanics*, 1979, **19**, 290-308.

101. I. Amidror, *The Theory of the Moiré Phenomenon: Vol. I: Periodic layers, 2nd ed.*, Springer, London, UK, 2009.
102. Z. Wu and Y. Zheng, *Advanced Optical Materials*, 2018, **6**, 1701057.
103. S. M. Lubin, A. J. Hryn, M. D. Huntington, C. J. Engel and T. W. Odom, *ACS Nano*, 2013, **7**, 11035-11042.
104. L. A. Ibbotson, A. Demetriadou, S. Croxall, O. Hess and J. J. Baumberg, *Sci Rep*, 2015, **5**, 8313.
105. Z. Wu and Y. Zheng, *Advanced Optical Materials*, 2017, **5**, 1700034.
106. S. M. Lubin, W. Zhou, A. J. Hryn, M. D. Huntington and T. W. Odom, *Nano letters*, 2012, **12**, 4948-4952.
107. J. H. Han, I. Kim, J. W. Ryu, J. Kim, J. H. Cho, G. S. Yim, H. S. Park, B. Min and M. Choi, *Opt. Express*, 2015, **23**, 17443-17449.
108. R. A. Harris, *The Journal of Chemical Physics*, 1965, **43**, 959-970.
109. A. O. Govorov and Z. Y. Fan, *Chemphyschem*, 2012, **13**, 2551-2560.
110. A. Ben-Moshe, B. Maoz, A. O. Govorov and G. Markovich, *Chem Soc Rev*, 2013, **42**, 7028-7041.
111. N. Engheta and P. Pelet, *Optics Letters*, 1989, **14**, 593-595.
112. N. A. Abdulrahman, Z. Fan, T. Tonooka, S. M. Kelly, N. Gadegaard, E. Hendry, A. O. Govorov and M. Kadodwala, *Nano letters*, 2012, **12**, 977-983.
113. C. Kramer, M. Schaferling, T. Weiss, H. Giessen and T. Brixner, *Acs Photonics*, 2017, **4**, 396-406.
114. Z. Y. Fan and A. O. Govorov, *Nano letters*, 2010, **10**, 2580-2587.
115. A. O. Govorov, *J Phys Chem C*, 2011, **115**, 7914-7923.
116. J. M. Slocik, A. O. Govorov and R. R. Naik, *Nano letters*, 2011, **11**, 701-705.
117. X. Shen, C. Song, J. Wang, D. Shi, Z. Wang, N. Liu and B. Ding, *Journal of the American Chemical Society*, 2011, **134**, 146-149.
118. P. Banzer, P. Woźniak, U. Mick, I. De Leon and R. W. Boyd, *Nature communications*, 2016, **7**, 13117.
119. M. Hentschel, M. Schaferling, B. Metzger and H. Giessen, *Nano letters*, 2013, **13**, 600-606.
120. S. Ohno, *Applied Physics Letters*, 2016, **108**, 251104.
121. F. Alali, Y. H. Kim, A. Baev and E. P. Furlani, *Acs Photonics*, 2014, **1**, 507-515.
122. B. K. Canfield, S. Kujala, M. Kauranen, K. Jefimovs, T. Vallius and J. Turunen, *Applied Physics Letters*, 2005, **86**.
123. B. K. Canfield, S. Kujala, K. Laiho, K. Jefimovs, J. Turunen and M. Kauranen, *Opt. Express*, 2006, **14**, 950-955.
124. L. Wang, H. F. Hu, K. Liu, S. H. Jiang, W. Zeng and Q. Q. Gan, *Plasmonics*, 2013, **8**, 733-740.
125. J. Zhou, J. Dong, B. Wang, T. Koschny, M. Kafesaki and C. M. Soukoulis, *Physical Review B*, 2009, **79**, 121104.
126. Y. Zhao, A. N. Askarpour, L. Sun, J. Shi, X. Li and A. Alu, *Nature communications*, 2017, **8**, 14180.
127. S. Takahashi, T. Tajiri, Y. Ota, J. Tatebayashi, S. Iwamoto and Y. Arakawa, *Applied Physics Letters*, 2014, **105**, 051107.
128. S. Takahashi, T. Tajiri, Y. Ota, J. Tatebayashi, S. Iwamoto and Y. Arakawa, *Applied Physics Letters*, 2014, **105**.
129. S. Takahashi, Y. Ota, T. Tajiri, J. Tatebayashi, S. Iwamoto and Y. Arakawa, *Physical Review B*, 2017, **96**.

130. W. S. Gao, H. M. Leung, Y. H. Li, H. Chen and W. Y. Tam, *J Optics-Uk*, 2011, **13**.
131. J.-G. Yun, S.-J. Kim, H. Yun, K. Lee, J. Sung, J. Kim, Y. Lee and B. Lee, *Opt. Express*, 2017, **25**, 14260-14269.
132. Z. L. Cao, L. Y. Yiu, Z. Q. Zhang, C. T. Chan and H. C. Ong, *Physical Review B*, 2017, **95**.
133. C. Genet and T. W. Ebbesen, *Nature*, 2007, **445**, 39-46.
134. T. Cao, C. Wei and L. Zhang, *Opt. Mater. Express*, 2014, **4**, 1526-1534.
135. S. P. Rodrigues, S. Lan, L. Kang, Y. Cui, P. W. Panuski, S. Wang, A. M. Urbas and W. Cai, *Nature Communications*, 2017, **8**, 0.
136. C. J. Kim, A. Sanchez-Castillo, Z. Ziegler, Y. Ogawa, C. Noguez and J. Park, *Nature Nanotechnology*, 2016, **11**, 520-+.
137. S. Kim, F. Shafiei, D. Ratchford and X. Li, *Nanotechnology*, 2011, **22**, 115301.
138. M. Kim, S. Lee, J. Lee, D. K. Kim, Y. J. Hwang, G. Lee, G. R. Yi and Y. J. Song, *Opt. Express*, 2015, **23**, 12766-12776.
139. M. Hentschel, M. Schaferling, X. Duan, H. Giessen and N. Liu, *Sci Adv*, 2017, **3**, e1602735.
140. A. J. Mastroianni, S. A. Claridge and A. P. Alivisatos, *Journal of the American Chemical Society*, 2009, **131**, 8455-8459.
141. B. Frank, X. Yin, M. Schaferling, J. Zhao, S. M. Hein, P. V. Braun and H. Giessen, *ACS Nano*, 2013, **7**, 6321-6329.
142. X. Z. Ye and L. M. Qi, *Nano Today*, 2011, **6**, 608-631.
143. T. Huang, Q. A. Zhao, J. Y. Xiao and L. M. Qi, *Acs Nano*, 2010, **4**, 4707-4716.
144. C. Jack, A. S. Karimullah, R. Tullius, L. K. Khorashad, M. Rodier, B. Fitzpatrick, L. D. Barron, N. Gadegaard, A. J. Lapthorn, V. M. Rotello, G. Cooke, A. O. Govorov and M. Kadodwala, *Nature Communications*, 2016, **7**, 10946.
145. A. S. Karimullah, C. Jack, R. Tullius, V. M. Rotello, G. Cooke, N. Gadegaard, L. D. Barron and M. Kadodwala, *Advanced Materials*, 2015, **27**, 5610-5616.
146. L. A. Nguyen, H. He and C. Pham-Huy, *International Journal of Biomedical Science : IJBS*, 2006, **2**, 85-100.
147. A. Calcaterra and I. D'Acquarica, *J Pharm Biomed Anal*, 2017, DOI: 10.1016/j.jpba.2017.07.008.
148. H. H. Jeong, A. G. Mark, M. Alarcon-Correa, I. Kim, P. Oswald, T. C. Lee and P. Fischer, *Nature Communications*, 2016, **7**, 11331.
149. J. Y. Ou, E. Plum, J. Zhang and N. I. Zheludev, *Nat Nanotechnol*, 2013, **8**, 252-255.
150. A.-K. U. Michel, P. Zalden, D. N. Chigrin, M. Wuttig, A. M. Lindenberg and T. Taubner, *ACS Photonics*, 2014, **1**, 833-839.

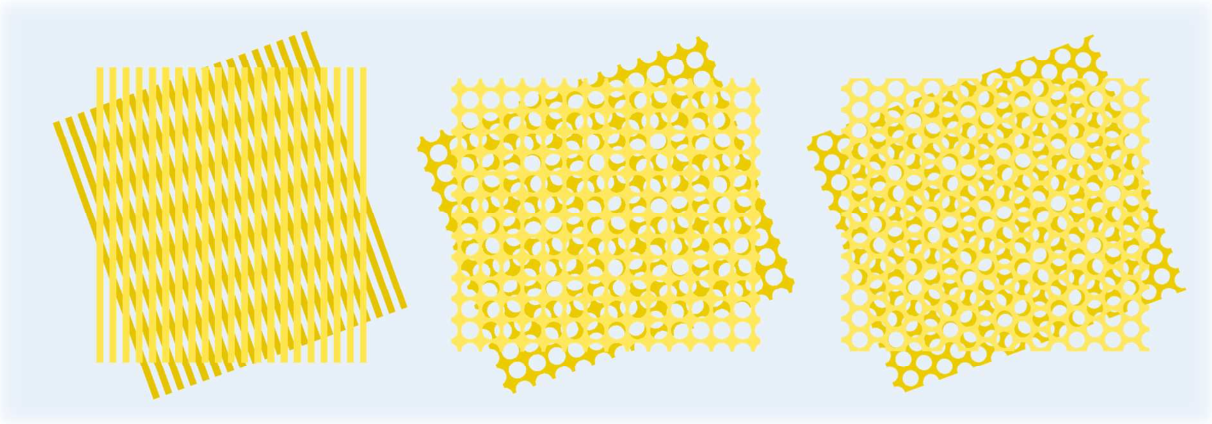

With their highly tunable chiroptical responses in combination with cost-effective and scalable fabrication, chiral metamaterials via moiré stacking are promising for a wide range of applications.